X-ray emission by a high-energy electron with a nonequilibrium field in an ultrathin crystal

S. V. Trofymenko*

Akhiezer Institute for Theoretical Physics of NSC "Kharkiv Institute of Physics and Technology" 1 Akademichna st., 61108 Kharkiv, Ukraine and Karazin Kharkiv National University, 4 Svobody sq., 61022 Kharkiv, Ukraine

(Received 29 March 2018; published 8 August 2018)

The process of coherent x-ray emission by an ultrarelativistic electron crossing a system of two targets, thick amorphous upstream and ultrathin crystalline downstream, is considered. It is shown that transformation of the electromagnetic field around the particle after its emission from the upstream target influences upon characteristics of radiation produced by the electron in the downstream target. The considered radiation is an interfering sum of parametric x-ray radiation and diffracted transition radiation. It is demonstrated that in the present case the properties of the x-ray pulse differ both from the ones typical for thick and ultrathin crystals and depend on the distance between the targets. At multi-GeV electron energies, such dependence is observable within macroscopically large values of this distance. Special attention is drawn to the study of the influence of the downstream target finiteness on radiation characteristics. It is shown that it results in the dependence of radiation yield on separation between the targets for macroscopically large values of such separation even at sub-GeV electron energies.

DOI: 10.1103/PhysRevA.98.023813

I. INTRODUCTION

When a relativistic charged particle moves through crystalline medium it emits different types of electromagnetic radiation which characteristics depend on the particle energy, polarization, and crystal alignment (see, e.g., [1–5]). They particularly include incoherent bremsstrahlung, Cherenkov, characteristic and transition radiation, which are also typical for amorphous media, as well as several types of radiation owing their origin to periodicity of the atomic arrangement. The latter ones are represented, for instance, by coherent bremsstrahlung, channeling radiation, and parametric x radiation. The first two of these types require proper orientation of crystallographic axes or planes with respect to the particle velocity. The properties of such emissions are defined by the shape of the particle trajectory (in classical consideration) which should have sufficiently small inclination angles with respect to a crystalline axis or plane. Parametric x-ray radiation (PXR), on the contrary, can be emitted at wide range of crystal orientations. It is a radiation of polarization type (like transition or Cherenkov ones) and can be emitted even at uniform and rectilinear particle motion through crystal (if neglect radiation recoil). It is the very type of radiation which we consider in this paper.

PXR is also a radiation of resonance type which pulse is formed by a large number of parallel periodically arranged crystallographic atomic planes which an impinging particle (for certainty we will talk about electron) successively crosses during its motion through crystal. The electron's Coulomb field polarizes the atoms of each plane causing them to radiate. The waves emitted by different planes interfere with each other (coherently amplifying) resulting in a nearly monochromatic pulse. It has a narrow angular distribution around the direction specular to the electron velocity with respect to the planes (we will further call it specular direction). The resonant frequency of PXR is close to the Bragg frequency of x rays diffracted in the corresponding direction. In this respect, the phenomenon of PXR is closely connected to the one of x-ray diffraction in crystals. However, presently we deal with diffraction of virtual photons of the electron's proper field instead of real electromagnetic waves. The considered radiation pulse formed of Bragg-diffracted field is usually called a reflex.

The first consideration of resonance radiation by fast particles in artificial periodic structures was presented in [6] for relatively long wavelengths. The theory of such radiation in crystals at wavelengths comparable to the interatomic distance (x-ray region) was built in [1]. In this book the expression for PXR spectral-angular density was derived with the use of kinematical approach, based on perturbative solution of Maxwell's equations. The analogous expression was further obtained in [7] applying quantum considerations. The dynamical theory of the effect, accounting for multiple diffraction of radiated waves on the system of crystallographic planes, was presented in [8,9].

First observations of PXR were reported in [10,11] and inspired further experimental investigation of this phenomenon (see [12–14] and references therein). A series of both experimental and theoretical studies was, particularly, devoted to investigation of dynamical diffraction effects in PXR (i.e., appearance of radiation pulse along the direction of particle velocity) [15–18] and correspondence between kinematical and dynamical treatment of the effect (see [19–21] and references therein).

PXR is produced in the bulk of a crystal. When an electron just enters this bulk from outside, it emits transition radiation as well. At ultrarelativistic energies of the particle certain part of this radiation belongs to x-ray range and undergoes

*trofymenko@kipt.kharkov.ua

Bragg diffraction inside a boundary layer of the crystal volume. The frequencies and propagation direction of such diffracted transition radiation (DTR) [4,20,22–24], defined by Bragg's law, are very close to the ones of PXR. At sufficiently high electron energies, the DTR differential yield at maximum of its angular distribution can significantly exceed the corresponding yield of PXR [25].

In [26,27] it was proposed to use PXR for the purposes of charged particle beam diagnostics in the region of their parameters (submicron beam size), where other techniques are inapplicable. Such idea was experimentally verified [28] and is being further elaborated (see, e.g., [25]). This makes further comprehensive study of radiation of this type highly required.

Existence of boundary effect for PXR in the form of DTR leads to the fact that the properties of x-ray emission by an ultrarelativistic electron in ultrathin and thick crystals are different [20,29]. By ultrathin crystals we mean here the ones of thickness in the direction of the particle motion less than about 1 μm (for more thorough definition, see Sec. II). Namely, in thick crystals the so-called density effect takes place for PXR. It occurs in the result of polarization of substance by the electron's proper Coulomb field, which leads to the screening of this field on distances $\rho > 1/\omega_p$ from the particle trajectory. Here, ω_p is the plasma frequency of the substance and we use a system of units in which the speed of light is $c = 1$. This effect manifests itself in saturation of PXR yield with the increase of the electron energy ϵ at $\gamma \sim \omega/\omega_p$ (here $\gamma = \epsilon/m$ is the electron Lorenz factor, m is the electron mass, and ω is the radiation frequency) and the energy independence of such yield at larger γ. Moreover, in this case the position of the maximum of PXR reflex angular distribution is defined by ω_p and does not depend on ϵ as well.

As shown [29] (see also corresponding remarks in [20]), in sufficiently thin crystals the density effect is completely absent. In this case, the position of the maximum of x-ray reflex angular distribution is defined by γ and significantly differs from the corresponding position in the case of thick crystal. The radiation yield in this case does not saturate and grows with the increase of ϵ at arbitrary values of this quantity.

In this paper, we consider a case in which characteristics of x-ray reflex produced by a high-energy electron traversing a single-crystalline target are not typical neither for thick nor for thin crystal. Such situation, for instance, takes place if the particle traverses a system of two targets, thick amorphous upstream and thin single-crystalline downstream, separated by a certain distance one from another. After the electron traversal of the thick target, the electromagnetic field around the particle becomes significantly suppressed comparing to the Coulomb field in vacuum. In the result of subsequent process of the electron's field regeneration, transition radiation (TR) appears. Such regeneration does not occur instantly but takes place within the distance from the target defined by the formation length of TR process [3,4,30,31]. At sufficiently high electron energies, this distance can be macroscopically large even in x-ray band and the downstream crystalline target can be placed within it. In this region, the field around the impinging particle significantly differs from the Coulomb one. It is manifested in the properties of x-ray reflex produced by the electron in the crystal, provided it is sufficiently thin. This work is devoted to the study of such properties.

Special attention here is also paid to investigation of the influence of the crystalline target transversal size finiteness on radiation characteristics in the considered case. It is shown that it causes variation of the observable radiation yield with the increase of separation between the targets even for separations significantly exceeding the formation length. Such separations can be macroscopically large even at not very high (sub-GeV) electron energies.

II. X-RAY EMISSION IN THICK AND ULTRATHIN CRYSTALS

In this paper, we will mainly focus on the crystals of thickness less than extinction length for x-ray photons. In this case, it is possible [20] to neglect the effects of dynamic diffraction, as well as radiation absorption, and apply kinematic treatment of x-ray emission process. Let us, by the way, note that in [7,19,21] it is argued that characteristics of PXR pulse in the vicinity of the Bragg angle are fairly well described by kinematic theory even for much thicker targets.

We follow the approach developed in [1], where it was applied for the case of a boundless crystal. In this section on the basis of the same kinematic approach the case of an ultrathin crystal (a case of a single target) is considered as well. We regard it as a test for the applied approach comparing the result with the one obtained in [29] in the framework of the dynamic theory.

A. Thick (quasi-infinite) crystal

In [1] the dielectric permittivity of the crystal is taken in the form

$$\varepsilon(\omega, \mathbf{r}) = \varepsilon_0(\omega) + \varepsilon'(\omega, \mathbf{r}). \tag{1}$$

Here, ε_0 is the mean macroscopic part of the permittivity, which at frequencies sufficiently higher than characteristic atomic ones equals

$$\varepsilon_0(\omega) = 1 - \omega_p^2/\omega^2. \tag{2}$$

The second term in (1) describes the periodically varying microscopic part of permittivity. It is proportional to the difference between the local microscopic atomic electron density and its macroscopic average value. It is assumed that $|\varepsilon'| \ll \varepsilon_0$ and the Maxwell's equations for the field created by the electron traversing the crystal are solved with the use of perturbation theory.

The leading-order (i.e., zeroth order in ε') solution of these equations in the present case is just the particle's proper field in a polarized matter, which (its Fourier component) in ultrarelativistic case can be presented as follows:

$$\mathbf{E}_\omega^{(0)}(\mathbf{r}) = -\frac{ie}{\pi}\int d^2q\, \mathbf{q} Q_c e^{i\omega z/v + i\mathbf{q}\cdot\boldsymbol{\rho}}. \tag{3}$$

Here, the particle with the charge e moves along the z axis with the velocity v; $\boldsymbol{\rho}$ is the observation point radius vector in the xy plane perpendicular to the z axis and $Q_c = 1/(q^2 + \omega_p^2 + \omega^2/\gamma^2)$. Let us note that here and further in the integral prefactor we omit the quantity ε_0 which is close to unit in the considered frequency range. The integration in (3) is made with

respect to the wave vectors $\mathbf{q}$ of the electron Coulomb field in xy plane ($|\mathbf{q}| = q$).

It is convenient to present the field scattered on the permittivity perturbation ε' (which is PXR field) in the form of decomposition over reciprocal lattice vectors $\mathbf{g}$ of the crystal. After the same procedure for ε',

$$\varepsilon'(\omega, \mathbf{r}) = \sum_{\mathbf{g}} n_{\mathbf{g}} e^{i\mathbf{g}\cdot\mathbf{r}}, \tag{4}$$

the required field, being the next-to-leading order solution of the Maxwell's equations, acquires the form

$$\mathbf{E}'_{\omega}(\mathbf{r}) = -\frac{e^{ikr}}{4\pi r} \sum_{\mathbf{g}} n_{\mathbf{g}} \mathbf{k} \times [\mathbf{k} \times \mathbf{I}_{\mathbf{g}}], \tag{5}$$

where

$$\mathbf{I}_{\mathbf{g}} = \int d^3 r' \mathbf{E}^{(0)}_{\omega}(\mathbf{r}') e^{i(\mathbf{g}-\mathbf{k})\cdot\mathbf{r}'}$$

and $\mathbf{k} = \omega\sqrt{\varepsilon_0}\mathbf{r}/r$ is the wave vector of the scattered (radiated) field inside the crystal. Let us note that here and further we neglect small difference of $\mathbf{k}$ from the wave vector of radiation after its escape from the crystal. The integration here is performed over the crystal volume. The Fourier components $n_{\mathbf{g}}$ of the quantity ε' are defined by the parameters of the crystal lattice (see, i.e., [4]). Expression (5) describes the field in the far-field zone where $|\mathbf{r}| \gg |\mathbf{r}'|$. With the use of (3) and the relation between the radiation field and its spectral-angular distribution

$$\frac{d^2 W}{d\omega\, do} = \frac{r^2}{4\pi^2} |\mathbf{E}'_{\omega}|^2 \tag{6}$$

the following expression is obtained for the latter characteristic of PXR (which is an ultrarelativistic limit of general results [1,7]):

$$\frac{d^2 W}{d\omega\, do} = \frac{e^2 L}{2\pi} \sum_{\mathbf{g}} |n_{\mathbf{g}}|^2 \frac{|\mathbf{k} \times [\mathbf{k} \times \boldsymbol{\kappa}_{\perp}]|^2}{(\kappa_{\perp}^2 + \omega_p^2 + \omega^2/\gamma^2)^2} \delta(\omega - \boldsymbol{\kappa}\boldsymbol{v}), \tag{7}$$

where $\boldsymbol{\kappa} = (\boldsymbol{\kappa}_{\perp}, \kappa_z) = \mathbf{k} - \mathbf{g}$ and L is the crystal thickness along the particle velocity (which is assumed to be less than radiation attenuation length in the target). $\delta(x)$ is the delta function which imposes a relation between radiation direction, defined by a unit vector $\mathbf{n}$, and frequency as

$$\omega_{\mathrm{PXR}} = \frac{|\boldsymbol{v}\mathbf{g}|}{1 - \sqrt{\varepsilon_0}\boldsymbol{v}\mathbf{n}}. \tag{8}$$

Note that ε_0 here is a function (2) of frequency and (8) should be considered as an equation for ω_{PXR}. Further, we will consider just the radiation peaks of the lowest order, corresponding to $|\mathbf{g}| = 2\pi s/a$ with the positive integer s equal unit. Here, a is the interplanar distance.

Integration over $\boldsymbol{\rho}'$ in (5) created another delta function $\delta(\mathbf{q} - \boldsymbol{\kappa}_{\perp})$ as well, which made possible direct integration over $\mathbf{q}$. The two considered delta functions together define the well-known relation between $\mathbf{k}$ and the wave vector of the initial virtual photon of the electron's Coulomb field $\mathbf{k}_i = (\mathbf{q}, \omega/v)$, which undergoes Bragg diffraction, as $\mathbf{k} = \mathbf{k}_i + \mathbf{g}$. Hence, narrow angular distribution of the vectors $\mathbf{k}_i$ around the direction of the electron velocity, following from (3), generates the analogous narrow angular distribution of the reflex around the specular direction (Fig. 1). At $\gamma \gg \omega/\omega_p$, its characteristic angular width is $\sim\omega_p/\omega$.

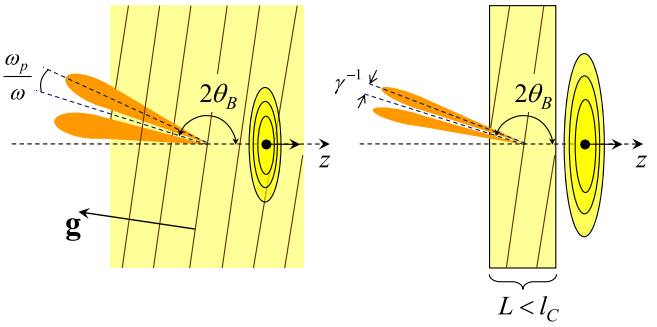

FIG. 1. Angular diagrams of x-ray reflexes produced by electron traversing thick (quasi-infinite) and ultrathin crystals.

It is necessary to note that the frequency ω experiences some change with the change of the observation angle within the reflex, according to (8). From a theoretical point of view, with the increase of frequency resolution of measurement the angular width of the observed peak at fixed frequency becomes smaller, while in the ideal case of monochromatic radiation from an infinite crystal it is described by the delta function in (7). The mentioned reflex of angular width $\sim\omega_p/\omega$ is an envelope comprising such peaks (see Fig. 2) in the corresponding small range of frequencies. However, having a finite (not infinitely small) size, the real detector catches a certain range of frequencies corresponding [via (8)] to the domain of the detector angular acceptance. Therefore, it is usually the angular distribution of the whole reflex which is discussed, but not the one of quasimonochromatic peaks. Nevertheless, further we will have to consider the latter one as well in order to judge on the possibility of interference between PXR and DTR contributions in an ultrathin crystal.

Let us note that further, referring to radiation from a thick crystal, it is PXR that we will talk about, not taking into account DTR from the entrance border of the crystal. At high electron energies these two types of radiation have different angular regions of concentration and can be in principle separated one from another.

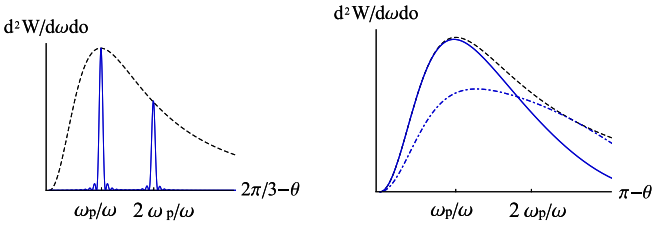

FIG. 2. Angular distributions of radiation spectral density associated with the first term (pure PXR) in (13). Left: $2\theta_B = 2\pi/3$; $\omega \approx 3.745$ keV (left peak), $\omega \approx 3.763$ keV (right peak). Right: $2\theta_B = \pi$; $\omega \approx 3.228$ keV (solid line), $\omega \approx 3.2285$ keV (dashed-dotted line). Dashed line represents the envelope comprising monochromatic peaks at different ω (its shape fits the reflex angular distribution with characteristic width $\sim\omega_p/\omega$).

B. Ultrathin crystal

Let us now consider the case of an ultrathin crystal. Here, strictly speaking, the quantity $\varepsilon'(\omega, \mathbf{r})$ should be decomposed into a Fourier integral, not a series. However, we will assume the representation (4) to be valid, as well as in an infinite crystal, since we are interested in targets still possessing more than 1000 atomic layers. Expression (5) can be also applied for calculation of radiation field in the considered case. However, presently the leading-order solution for the electric field, i.e., the field which takes place if $\varepsilon(\omega, \mathbf{r}) = \varepsilon_0(\omega)$ inside the target and $\varepsilon(\omega, \mathbf{r}) = 1$ outside it, is different from (3). Now, together with (3), it also includes transition radiation (TR) generated upon the particle traversal of crystal boundaries.

For definiteness, let us consider the process in Bragg geometry, as shown in Fig. 1, and presume normal electron incidence on the surface. In order to find the leading-order solution for the total field inside the crystal at ultrarelativistic energies of the impinging electron, it is enough to take into account just the contribution of an upstream boundary to TR field, neglecting the one of the downstream. Solution of the Maxwell's equations with the boundary conditions for electric field on the upstream surface leads to the following expression for this field:

$$\mathbf{E}^{(0)}_{\omega}(\mathbf{r}) = -\frac{ie}{\pi}\int d^2q\,\mathbf{q}\{Q_c e^{i\frac{\omega z}{v}} + Q_f e^{iz\sqrt{\omega^2\varepsilon_0 - q^2}}\}e^{i\mathbf{q}\cdot\boldsymbol{\rho}}, \tag{9}$$

where

$$Q_f = 1/(q^2 + \omega^2/\gamma^2) - 1/(q^2 + \omega_p^2 + \omega^2/\gamma^2). \tag{10}$$

Substituting (9) into (5) and integrating it with respect to $\mathbf{q}$ and $\boldsymbol{\rho}'$ (presently we consider a crystal of infinite transversal size, so that $0 < |\boldsymbol{\rho}'| < \infty$), as well as with respect to z' in the range $0 < z' < L$ for the field of the x-ray pulse, we obtain

$$\mathbf{E}'_{\omega}(\mathbf{r}) = ie\frac{e^{ikr}}{r}\sum_{\mathbf{g}} n_{\mathbf{g}}\mathbf{k}\times[\mathbf{k}\times\boldsymbol{\kappa}_{\perp}] \times\left\{\mathrm{K}_c e^{iLq_c/2}\frac{\sin(Lq_c/2)}{q_c/2} + \mathrm{K}_f e^{iLq_f/2}\frac{\sin(Lq_f/2)}{q_f/2}\right\}, \tag{11}$$

where $q_f = \sqrt{\omega^2\varepsilon_0 - \boldsymbol{\kappa}_{\perp}^2} - \kappa_z, q_c = \omega/v - \kappa_z$, while $K_{c,f}$ are defined by the same expressions as $Q_{c,f}$ with the substitution $q^2 \to \boldsymbol{\kappa}_{\perp}^2$.

The first term in (11) describes the field of the same nature as in infinite crystal. It is generated in the result of scattering of the electron's proper Coulomb field [first term in (9)] on periodical inhomogeneity ε' of permittivity. The second term describes the Bragg-diffracted TR field.

If the condition $L < 1/|q_c - q_f|$ is fulfilled, we may neglect the difference between q_c and q_f in the sine arguments and exponents in (11) and present the expression in braces in the following form:

$$K'_c e^{iLq_c/2}\frac{\sin(Lq_c/2)}{q_c/2},$$

with $K'_c = 1/(\boldsymbol{\kappa}_{\perp}^2 + \omega^2/\gamma^2)$. It coincides with the first term in (11) if set $\omega_p \to 0$ there. It indicates that under the considered condition for crystal thickness, the polarization of the target does not affect radiation characteristics and the density effect is absent, which is in accordance with corresponding statements in [20,29]. Such effect of suppression of polarization influence upon electromagnetic processes in ultrathin targets has analogs in the processes of ionization loss [32–34] and K-shell excitation (see [35] and references therein). After slight transformations, the mentioned condition for L can be rewritten in the form

$$L < \frac{2}{\omega(\gamma^{-2} + \omega_p^2/\omega^2 + \boldsymbol{\kappa}_{\perp}^2/\omega^2)} = l_c, \tag{12}$$

were l_c is TR coherence (formation) length inside the target. In the targets of such thickness PXR and DTR fields, described respectively by the first and the second terms in (11), significantly interfere and should be considered as a single inseparable x-ray pulse. It is such crystals that we name here ultrathin. At frequencies $\sim$1 keV l_c reaches the value $\sim$1 μm.

With the use of (11) and (6) the expression for radiation spectral angular density can be directly obtained:

$$\frac{d^2W}{d\omega\,do} = \frac{e^2\omega^2}{4\pi^2v^2}\sum_{\mathbf{g}}|n_{\mathbf{g}}|^2|\mathbf{k}\times\boldsymbol{\kappa}_{\perp}|^2\big\{K_c^2S_c^2 + K_f^2S_f^2 + 2K_cK_fS_cS_f\cos[L(q_f - q_c)/2]\big\}, \tag{13}$$

where we denoted $S_{c,f} = \sin(Lq_{c,f}/2)/(q_{c,f}/2)$. For targets satisfying the condition (12) the expression in braces simplifies to $K_c'^2S_c^2$ making (13) analogous to the result obtained in [29]. The characteristic angular width of the pulse in this case is $\sim\gamma^{-1}$ at arbitrary energies of the impinging relativistic electron.

Peak width and possibility of PXR and DTR interference in an ultrathin crystal

Generally speaking, in (13) it is not possible to make substitution

$$S_{c,f}^2 \to 2\pi L\delta(q_{c,f}) \tag{14}$$

like in (7). The finite small thickness of the target in this case leads to widening of the radiation peak angular and frequency distributions. Let us discuss spectral and angular widths of such peak in the considered ultrathin target more thoroughly. For simplicity of our estimations, we will presently consider radiation in the plane of vectors $\boldsymbol{v}$ and $\mathbf{g}$.

The discussed widths are defined by the factors $S_{c,f}$ in (13). The region of a peak approximately corresponds to the range $-2\pi/L < q_c, q_f < 2\pi/L$ of the sine arguments in these factors. The quantity $q_c = \omega(1 - \sqrt{\varepsilon_0}v\cos\theta) + \mathbf{g}\boldsymbol{v}$, where θ is the angle between $\mathbf{k}$ and $\boldsymbol{v}$, is zero under condition (8). Let us make here small-angle variation $\delta\vartheta/2$ leaving the frequency intact. Requiring that corresponding variation of q_c equals $2\pi/L$ the peak angular width, associated with S_c, can be obtained as

$$\delta\vartheta \sim \frac{4\pi}{\omega L\sin\theta}. \tag{15}$$

Let us note that presently we consider the peak angular width (15), presenting a merely theoretical interest, in order to investigate the possibility of interference of PXR and DTR contributions in the present case. Such interference is possible if the corresponding peaks of these types of emission have

sufficient width to overlap both in the angular and the frequency domains. The value (15) should not be confused with the reflex angular size ($\sim\omega_p/\omega$ for PXR and $\sim 1/\gamma$ for DTR) which is defined by the K_c^2 and K_f^2 terms in (13).

Further, the numerical estimations will be made for silicon targets ($\omega_p \approx 31$ eV) of thickness $L = 0.5$ μm. In this case, for instance, at $\omega \sim 3$ keV $\delta\theta \sim 10^{-3}/\sin\theta$. At θ far from π this width is noticeably smaller than $\omega_p/\omega \sim 10^{-2}$ and the substitution (14) is approximately valid for S_c. It is, however, not the case in the vicinity of backward radiation direction when $\pi - \theta \ll 1$. The substitution (14) is also inapplicable if we consider distribution (13) at angles $\sim\gamma^{-1}$ from the specular direction for $\gamma > 10^3$ since in this case $\delta\theta > \gamma^{-1}$. The examples of x-ray peak spectral-angular distribution, associated with the first term in (13), for different values of frequency and angle θ_B between $\boldsymbol{v}$ and the considered crystallographic plane (Bragg angle) are presented on Fig. 2 for $\gamma \gg \omega/\omega_p$. The dashed lines represent here the envelope comprising a continuous series of monochromatic peaks with slightly different frequencies corresponding to slightly different emission directions (the shape of such envelope coincides with the one of the frequency integrated angular distribution of the whole reflex). For definiteness here and further we consider a single term of the sum over $\mathbf{g}$ in (13) corresponding to (220) plane of Si crystal (and, as noted previously, the peak of the lowest order). In this case, the frequency $\omega_{\rm PXR}$ in the specular direction for $2\theta_B = 2\pi/3$ (left figure) is $\omega_{\rm PXR} \approx 3.727$ keV, while for $2\theta_B = \pi$ (right figure), which corresponds to backward radiation direction, it is $\omega_{\rm PXR} \approx 3.228$ keV. Here we see, in accordance with (15), rather sharp peaks in the first case, while in the second case, due to smallness of $\sin\theta$, the width of the peaks nearly coincides with the one $\sim\omega_p/\omega$ of the reflex.

By a small variation of ω in the expression for q_c, the minimum frequency width of radiation peak, caused by finiteness of the target thickness, can be obtained (since we do not consider the case $\theta \ll 1$ it is possible to put here $\varepsilon_0 = 1$):

$$\delta\omega \sim \frac{4\pi v}{L(1 - v\cos\theta)}, \tag{16}$$

which is in accordance with [2] and in the considered case ($L = 0.5$ μm) is about several eV. Thus, at crystal thickness under consideration the monochromaticity of radiation peak remains almost intact.

As noted previously, at the considered value of L the phases of the sines in S_c and S_f are close to each other. This makes the angular and frequency widths of radiation peaks associated with S_f close to (15) and (16). Figure 3 shows the comparison of radiation angular distributions in the considered case associated with the first (PXR) and second (DTR) terms in (13) at 200 MeV electron energy. The dashed and dotted-dashed lines represent the reflexes of DTR and PXR, respectively. As the figure shows, in the considered case the peaks angular width (15) for these types of emission is enough for them to overlap, despite their maxima correspond to slightly different angles. This fact stipulates the possibility of significant interference of PXR and DTR in the considered case, described by the third term in (13).

The analogous situation takes place if we compare spectral widths of the discussed peaks. Figure 4 shows the spectral distributions (normalized to equal height at their maxima

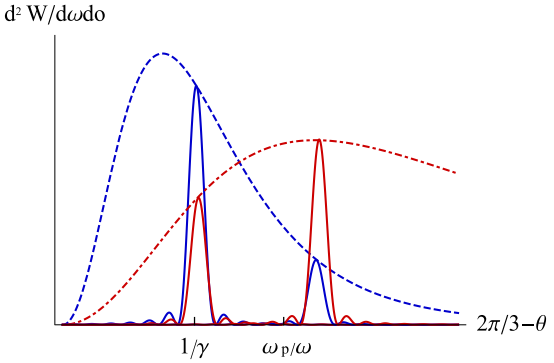

FIG. 3. Angular distributions of PXR and DTR from a crystal of thickness $L = 0.5$ μm for two values of frequency: 3.738 keV (left narrow peaks), 3.748 keV (right narrow peaks), and $\gamma = 200$, $2\theta_B = 2\pi/3$. Dashed and dotted-dashed lines are the reflexes of DTR and PXR, respectively.

positions) of PXR (solid line) and DTR (dashed line) terms of (13). Here, we see that at the considered value of L the width of the peaks significantly exceeds the shift between their maxima positions [the Bragg frequency $\omega_B = g^2/(2\sqrt{\varepsilon_0}\mathbf{gn})$ of DTR maximum, as usually, slightly exceeds $\omega_{\rm PXR}$], which allows presently to neglect the difference between ω_B and $\omega_{\rm PXR}$. The figure corresponds to the observation angle $\theta = 2\theta_B - \omega_p/\omega$ with $2\theta_B = 2\pi/3$. With the decrease of the $2\theta_B - \theta$ value, the difference $\omega_B - \omega_{\rm PXR}$ decreases even more. The presented considerations show that for the chosen thickness of the crystalline target the x-ray peaks still remain rather narrowly directed (except in the case $2\theta_B = \pi$) and monochromatic. Nevertheless, the peaks of PXR and DTR overlap both in angular and frequency domains and can interfere with each other.

Let us note that in this section we discussed the widening of radiation peaks associated only with the target finiteness and did not take into account the effects of finite detector resolution, electron multiple scattering, etc. The obtained results for the peak widths are also valid for the further considered case of the impinging electron with nonequilibrium field [the same quantities $S_{c,f}$ appear in the correspondent formulas (26) and (40)]. They will be used for defining the effective regions

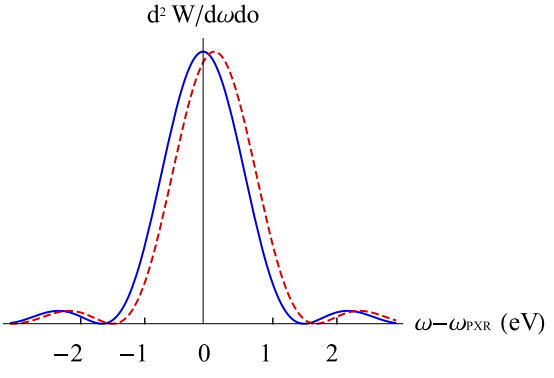

FIG. 4. Normalized spectral distributions of PXR (solid line) and DTR (dashed line) from thin crystal for $\theta = 2\theta_B - \omega_p/\omega$, where $2\theta_B = 2\pi/3$ and $\omega_{\rm PXR} \approx 3.745$ keV.

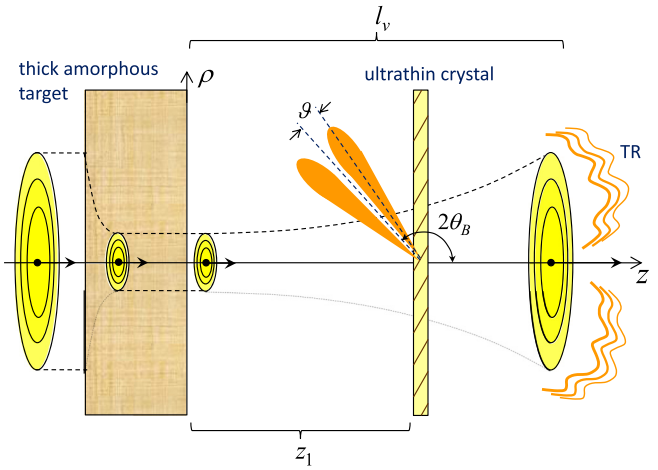

FIG. 5. Electron traversal of the system of two targets, thick amorphous upstream and thin crystalline downstream, and schematic picture of the accompanying field transformation.

of numerical integration in calculations of the frequency and angle-integrated signals in Secs. III B and IV.

III. EMISSION IN THE SYSTEM OF TWO TARGETS

In the previous section we discussed the properties of x-ray pulses emitted by an ultrarelativistic electron traversing thick and ultrathin crystalline targets. In both cases, the impinging electron was supposed to move uniformly rectilinearly in vacuum before hitting the target having equilibrium Coulomb field around it. In this section we study the influence of the nonequilibrium state of the field around the electron caused by the particle interaction with matter upon characteristics of x-ray pulse generated subsequently by the electron in an ultrathin crystal. As an example of process in which the electron field is modified, we choose the particle traversal of thick amorphous target (Fig. 5). In this case, due to TR formation process after the electron exit from the target the field around the particle can significantly differ from the Coulomb one within macroscopically large domain of space. As shown, this leads to modification of radiation characteristics from an ultrathin downstream crystalline target situated in this domain. The upstream target is assumed to be amorphous so that all crystal-assisted radiation could be associated with the downstream one.

A. Electric field of the particle inside the downstream thin target

According to (5), in order to define the required radiation characteristics, it is necessary to know the leading-order solution for the electric field in the target, which we consider in this section.

The field around the electron after its emission from the upstream target into vacuum can be calculated from the Maxwell's equations with the boundary conditions [1,31,36] on the target surface. Let us note that presently we take into account such conditions only on the downstream surface assuming the target to be thick enough (at least thicker than several microns) to absorb TR (at considered frequencies) emitted at the upstream one. The target is also supposed to be not very thick so that electron multiple scattering inside it, resulting in the particle deflection from the z axis, could be neglected. Let us denote the plasma frequency of the upstream target as η_p, while the one of the downstream target leave as ω_p. In ultrarelativistic case in the x-ray frequency region the field around the electron can be considered as approximately transversal to the electron velocity [as (9)] and presented in the form:

$$\mathbf{E}_\omega(\mathbf{r}) = -\frac{ie}{\pi}\int d^2q\,\mathbf{q}\left\{Q'_c e^{i\frac{\omega z}{v}} - Q'_f e^{iz\sqrt{\omega^2-q^2}}\right\}e^{i\mathbf{q}\cdot\boldsymbol{\rho}}, \quad (17)$$

where $Q'_c = 1/(q^2+\omega^2/\gamma^2)$ and $Q'_f = 1/(q^2+\omega^2/\gamma^2) - 1/(q^2+\eta_p^2+\omega^2/\gamma^2)$. The first term here describes the electron proper Coulomb field in vacuum while the second one is the free field gradually transforming into diverging waves of TR. Within the formation distance (12), which reaches the value $l_c \sim \gamma^2/\omega$ in vacuum, these fields are not separated one from another and significantly interfere.

Let us consider more thoroughly the evolution of the field (17) with the increase of the distance from the target. For this purpose, it is possible to expand the square root in the exponent of the second term and present it as $\sqrt{\omega^2-q^2} \approx \omega(1-q^2/2\omega^2)$. It is associated with smallness of the effective value of the ratio q/ω for q contributing to the integral in (17), which indicates the preferable direction of TR propagation to be close to the electron velocity.

The integrand in (17) depends on a single constant vector $\boldsymbol{\rho}$, which defines the direction of $\mathbf{E}_\omega$. The integral from the first term in (17) can be analytically calculated and represents the well-known expression for the Fourier component of the Coulomb field in vacuum:

$$\mathbf{E}^c_\omega(\mathbf{r}) = \frac{2e\omega}{\gamma}\frac{\boldsymbol{\rho}}{\rho}K_1\left(\frac{\omega\rho}{\gamma}\right)e^{i\omega z/v}, \quad (18)$$

where $K_1(x)$ is the Macdonald function.

After integration with respect to angle between $\mathbf{q}$ and $\boldsymbol{\rho}$, the second term in (17) can be presented as

$$\mathbf{E}^f_\omega(\mathbf{r}) = -2e\frac{\boldsymbol{\rho}}{\rho}e^{i\omega z}\int dq\,q^2 J_1(q\rho)Q'_f e^{-iq^2 z/2\omega}, \quad (19)$$

where $J_1(x)$ is the Bessel function. Let us consider a part of this expression associated with the first term of Q'_f (the one without η_p). With the use of a procedure, applied for the analogous integral, i.e., in [37] [formula (22)], it can be written as

$$2e\frac{\boldsymbol{\rho}}{\rho}e^{i\omega z}\left\{\frac{2i}{\rho}\sin\left(\frac{\omega\rho^2}{4z}\right)e^{i\omega\rho^2/4z} + \frac{1}{\rho} - \frac{\omega}{\gamma}K_1\left(\frac{\omega\rho}{\gamma}\right)\right\}. \quad (20)$$

Such representation is valid under condition $z \ll \gamma^2/\omega$. The similar expression (with the opposite sign) is obtained for the remainder of (19) associated with the second term of Q'_f. The only difference is the substitution $\omega/\gamma \to \sqrt{\omega^2/\gamma^2+\eta_p^2}$ in the third term in braces in (20). However, unlike (20), such analytical representation of the considered part of the expression (19) is valid at $z \ll \omega/\eta_p^2$. Under condition $\gamma \gg \omega/\eta_p$, which we are interested in, it is a stronger restriction than the one for (20). Substituting the obtained analytical

representations to (17), at $\gamma \gg \omega/\eta_p$ we have

$$\mathbf{E}_\omega(\mathbf{r}) = 2e\eta_p \frac{\boldsymbol{\rho}}{\rho} e^{i\omega z} K_1(\eta_p \rho). \tag{21}$$

This expression shows that even after the electron exit from the target, within the distance $z \sim \omega/\eta_p^2$ from it, the Fourier component of the total field around the particle has the same form as inside the target. Comparison of (21) with (18) shows that after the particle exit the Fourier components of frequencies $\omega < \gamma\eta_p$ are suppressed in the field (17) surrounding the electron and the corresponding virtual photons are almost absent in this field.

Such structure of the field resembles the one which takes place after a charged particle scattering on an atom in matter or its deflection in magnetic field. The effect of particle field suppression in this case, causing subsequent weakening of its interaction with the surrounding matter, was predicted in [38] and further discussed in [3,39,40]. In [38] the particle with such incomplete field was named "half-bare" particle. The study of the processes of this kind led to theoretical prediction and subsequent experimental observation of Landau-Pomeranchuk-Migdal [41–44] and Ternovsky-Shul'ga-Fomin [45–49] effects of suppression of bremsstrahlung by high-energy electrons in amorphous media. In [50,51], the observation of so-called diffraction radiation suppression (in millimeter wavelength range) was reported for the case when the radiating particle preliminarily "undressed" by moving close to a conducting screen. In [52,53], the effects associated with a particle field suppression were considered for radiation of particles traversing optical fibers and for Smith-Purcell radiation, while in [54–56] for transition radiation of half-bare particles. In [57,58], the related effects were studied for ionization loss of electrons and electron-positron pairs with nonequilibrium field in thin films. Further, we consider the effects of this kind for x-ray emission in ultrathin crystals.

Let us consider the field (17) on larger distances from the target at $\omega/\eta_p^2 \ll z \ll \gamma^2/\omega$. Within the distance $\rho \sim 1/\eta_p$ from the electron trajectory the field is not affected by polarization of the target and is defined by the formula (18) at arbitrary z. Therefore, we will focus on the case $\rho \gg 1/\eta_p$. In this region, the part of the expression (19) associated with the first term of Q'_f (without η_p) is defined by the analytical representation (20). The other part of the integral (19), associated with the second term of Q'_f, can be calculated with the use of stationary phase method [59]. In this case, the Bessel function here should be presented in its asymptotic form as $J_1(q\rho) \approx \sqrt{2/\pi q\rho}\cos(q\rho - 3\pi/4)$. The cosine, presented as the difference of exponents, according to Euler's formula, together with the exponent in the integrand of (19), provide a single stationary point $q_0 = \omega\rho/z$ on the integration interval. In the result the total field (17) around the electron in this case can be presented in the form

$$\mathbf{E}_\omega(\mathbf{r}) = 2e\frac{\boldsymbol{\rho}}{\rho} e^{i\omega z} \frac{\omega_p^2}{\omega_p^2 + (\omega\rho/z)^2} \frac{e^{i\omega\rho^2/2z}}{\rho}. \tag{22}$$

In the region $\rho \ll \sqrt{z/\omega}$ it coincides with (18) and represents the part of the Coulomb field which the electron has already managed to "regenerate" around itself. In the region $\rho > \sqrt{z/\omega}$ the TR field (19) is mainly concentrated and still significantly interferes with the electron proper field. The characteristic angles $\alpha = \rho/z$ of TR concentration in this case are $\sim\sqrt{1/\omega z}$ and decrease with the increase of z reaching their far-field value $1/\gamma$ at $z \sim \gamma^2/\omega$. At $\rho > z\omega_p/\omega$ the field (22) rapidly drops as $1/\rho^3$.

At $z \gg \gamma^2/\omega$ the whole integral (19) can be calculated with the use of stationary phase method like its single term in the previously considered case of smaller z. This directly leads to the following field asymptotic:

$$\mathbf{E}_\omega(\mathbf{r}) = 2e\frac{\boldsymbol{\rho}}{\rho}\left\{\frac{\omega}{\gamma}K_1\left(\frac{\omega\rho}{\gamma}\right)e^{i\frac{\omega z}{v}} + \frac{e^{i\omega r}}{r}A(\alpha)\right\}. \tag{23}$$

Here, we used the approximation $z + \rho^2/2z \approx r$, provided $\rho \ll z$, where $r = |\mathbf{r}|$. The presented expression indicates a complete separation of the field around the electron into proper Coulomb field and spherically diverging waves of TR at $z \gg \gamma^2/\omega$. The quantity (its square)

$$A(\alpha) = \frac{\eta_p^2}{\omega^2}\frac{\alpha}{(\alpha^2 + \gamma^{-2})(\alpha^2 + \eta_p^2/\omega^2 + \gamma^{-2})},$$

where $\alpha = \rho/z$, defines the well-known TR angular distribution in the far-field zone [31,36].

The field inside a thin crystalline target placed downstream with respect to the thick amorphous one can be calculated by insertion of the field (17) into the boundary condition for the electric field tangential component on the upstream side of the target. Let this side be situated in the plane $z = z_1$. The boundary condition in this case reads as $\mathbf{E}^v_\omega(\rho, z_1) = \mathbf{E}^t_\omega(\rho, z_1)$, where the left-hand side and right-hand side, respectively, denote the total fields in vacuum and target. As far as $\mathbf{E}^v$ is concerned, we will use the expression (17) for it. Thereby we neglect the waves propagating opposite to the z axis due to small reflection coefficient of the plate in x-ray region. We make the same approximation for $\mathbf{E}^t$ neglecting the influence of the downstream boundary upon the field inside the plate. The field $\mathbf{E}^t$ consists of the electron proper field in the plate, defined by the first term in (9), and the free field which can be presented as [1]

$$\mathbf{E}^{t(f)}_\omega(\mathbf{r}) = \frac{1}{(2\pi)^3}\int d^3k\, \mathbf{E}'^{t(f)}_{\omega,\mathbf{k}}\delta(\omega^2\varepsilon_0 - k^2)e^{i\mathbf{k}\cdot\mathbf{r}},$$

where $\mathbf{k} = (\mathbf{q}, k_z)$, and integrated with respect to k_z taking into account only the root $k_z = +\sqrt{\omega^2\varepsilon_0 - q^2}$ of the delta-function argument. Thereby the boundary condition gives the following form of the total field (leading-order solution) inside the target:

$$\mathbf{E}^{t(0)}_\omega(\mathbf{r}) = -\frac{ie}{\pi}\int d^2q\, \mathbf{q}e^{i\mathbf{q}\cdot\boldsymbol{\rho}}\Big\{Q_c e^{i\frac{\omega z}{v}} + [Q_f e^{i\frac{\omega z_1}{v}} - Q'_f e^{iz_1\sqrt{\omega^2-q^2}}]e^{i(z-z_1)\sqrt{\omega^2\varepsilon_0-q^2}}\Big\}. \tag{24}$$

Under condition (12), within the whole volume of the crystal ($z_1 \leqslant z \leqslant z_1 + L$) it becomes close to the nonequilibrium field (17) in vacuum at $z = z_1$, which falls on the target. Therefore, the evolution of the electron's field after its exit from substance, described in this section, should be directly manifested in the properties of radiation emitted by the particle in sufficiently thin downstream targets.

B. X-ray emission from the downstream ultrathin target

Let us consider the properties of x-ray pulse which is produced in the downstream ultrathin crystalline target in the discussed process (Fig. 5). The field of such pulse can be obtained by insertion of (24) into (5) and has the following form (we consider a single term of the sum over **g**):

$$\mathbf{E}'_{\omega}(\mathbf{r}) = ie\frac{e^{ikr}}{r}n_{\mathbf{g}}\mathbf{k}\times[\mathbf{k}\times\boldsymbol{\kappa}_{\perp}]\Big\{K_c S_c e^{i(z_1+\frac{L}{2})q_c} + S_f e^{i\frac{L}{2}q_f - iz_1\kappa_z}\Big[K_f e^{i\frac{\omega z_1}{v}} - K'_f e^{iz_1\sqrt{\omega^2-\boldsymbol{\kappa}_{\perp}^2}}\Big]\Big\}, \tag{25}$$

where K'_f equals Q'_f with substitution $q^2 \to \boldsymbol{\kappa}_{\perp}^2$.

The forms of the expressions for K_c, K_f, and K'_f indicate that the field (25) is far from zero only at small values of $\kappa_{\perp}$ comparing to ω. This allows decomposing the square root in the exponent and present the expression in square brackets in the form

$$K_f e^{i\frac{\omega z_1}{v}} - K'_f e^{iz_1\sqrt{\omega^2-\boldsymbol{\kappa}_{\perp}^2}} \approx e^{i\frac{\omega z_1}{v}}(K_f - K'_f e^{-iz_1/l_v}).$$

By l_v we denote here the vacuum formation length defined by (12) with $\omega_p = 0$.

With the use of (6) the expression for radiation spectral-angular density is obtained:

$$\frac{d^2W}{d\omega\, do} = \frac{e^2\omega^2}{4\pi^2}|n_{\mathbf{g}}|^2|\mathbf{k}\times\boldsymbol{\kappa}_{\perp}|^2\Big\{K_c^2S_c^2 + S_f^2\big|K_f - K'_f e^{-i\frac{z_1}{l_v}}\big|^2 + 2K_cS_cS_f\mathrm{Re}\Big[e^{iL(q_f-q_c)/2}\Big(K_f - K'_f e^{-i\frac{z_1}{l_v}}\Big)\Big]\Big\}. \tag{26}$$

At $z_1 \ll l_v$, provided (12) is fulfilled, the expression in braces is reduced to $S_c^2/(\kappa_{\perp}^2 + \eta_p^2 + \omega^2/\gamma^2)^2$. In this case, (26) is analogous to the distribution (7) and differs from it by the substitution $\omega_p \to \eta_p$ and the presence of S_c^2 instead of δ function according to the relation (14). This means that in this case the angular width of the reflex is influenced by the density effect even in the ultrathin target. However, the first difference ($\omega_p \to \eta_p$) indicates that presently such width is defined not by the plasma frequency ω_p of the crystalline target, as in (7), but by the one η_p of the upstream target. The second difference is caused by the small value of the crystalline target thickness, which widens the peak, unlike the case of (7) which corresponds to quasi-infinite target approximation.

Let us note that at $\gamma \gg \omega/\eta_p$ the value of l_v changes significantly within the reflex (it decreases with the increase of the observation angle ϑ counted from the direction $\kappa_{\perp} = 0$, being almost the specular one). Therefore, for different observation angles the condition $z_1 \ll l_v$ for the similarity between (26) and (7) is reached at different distances between the targets. The scale of characteristic maximum width of the considered reflexes is $\sim\eta_p/\omega$ (corresponding to $\kappa_{\perp}^{max} \sim \eta_p$). This allows to define the distance at which the expression (26) tends to (7) at arbitrary ϑ as $l_p \sim \omega/\eta_p^2$. It, naturally, coincides with the distance on which the field around the electron equals the one inside the thick target and is described by the formula (21). Under condition $z_1 < l_p$, and assuming (14), the reflex corresponding to (26) is the same as that of PXR in a quasi-infinite crystal (7), but with $\varepsilon_0 = 1 - \omega_p^2/\omega^2$ replaced by that of the amorphous target $1 - \eta_p^2/\omega^2$. If $\eta_p = \omega_p$, we have the complete equality between (26) and (7). Such case is considered for numerical estimations, which results are presented on figures.

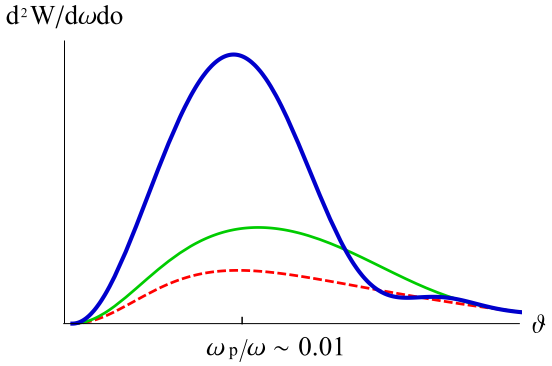

FIG. 6. Angular distributions of radiation spectral density (28) for $2\theta_B = \pi$ and $\gamma = 10^4$. Dashed line: distribution at $z_1 \ll l_p$ of the form $\vartheta^2/(\vartheta^2 + \omega_p^2/\omega^2)^2$; thin solid line: $z_1 = l_p$; thick solid line: $z_1 = 3l_p$.

With the increase of the distance between the targets, the radiation angular distribution gradually changes. The angular maximum of its reflex shifts to lower values, while the differential yield in this maximum grows. Figures 6 and 7 show the evolution of such angular distribution for the values of z_1 of the order of l_p and l_v, respectively, for electron energy $\epsilon = 5$ GeV. They depict the simplest case of $2\theta_B = \pi$ when crystallographic planes are parallel to the target surface. In this case, the corresponding constituents of the expression (26) can be presented in the form

$$|\mathbf{k}\times\boldsymbol{\kappa}_{\perp}|^2 = \omega^4\vartheta^2, \quad \kappa_{\perp}^2 = \omega^2\vartheta^2, \tag{27}$$

making (26) axially symmetric with respect to z axis. It is the case $\eta_p = \omega_p$ that is depicted on the figures, for which the expression (26) transforms to

$$\frac{d^2W}{d\omega\, do} = \frac{e^2\omega^6\vartheta^2}{4\pi^2}|n_{\mathbf{g}}|^2\Big\{K_c^2S_c^2 + 2K_f^2S_f^2[1-\cos(z_1/l_v)] + 2K_cK_fS_cS_f\mathrm{Re}\Big[e^{iL(q_f-q_c)/2}\Big(1 - e^{-iz_1/l_v}\Big)\Big]\Big\}. \tag{28}$$

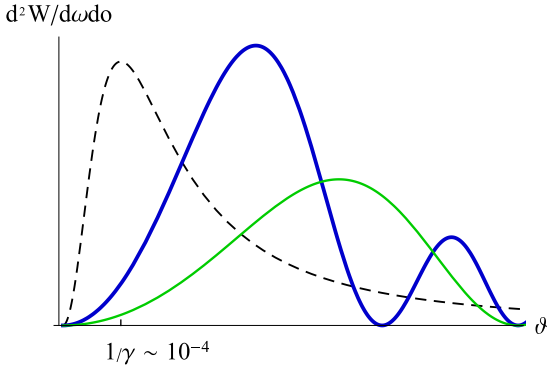

FIG. 7. The same as in Fig. 6. Thin solid line: $z_1 = 0.1l_v$; thick solid line: $z_1 = 0.2l_v$. Dashed line: distribution (13) in an ultrathin target for impinging electron with Coulomb field of the form $\vartheta^2/(\vartheta^2 + \gamma^{-2})^2$.

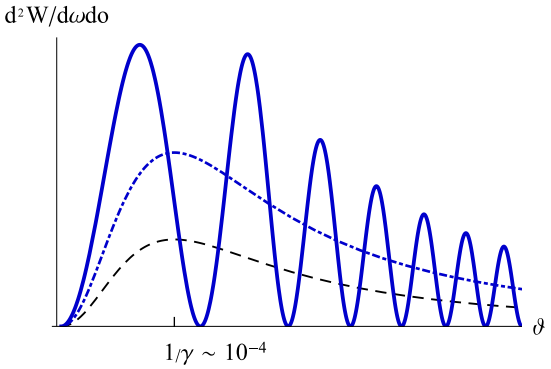

FIG. 8. The same as in Fig. 7. Dashed line: the same as in Fig. 7; dotted-dashed line: mean behavior of quickly oscillating distribution at $z_1 \gg l_v$; solid line: nonaveraged distribution for $z_1 = 2.5 l_v$.

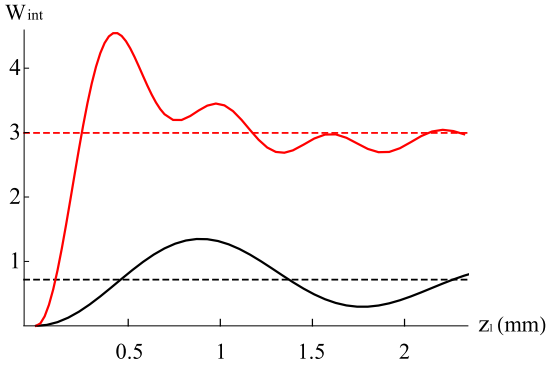

FIG. 9. Dependence of the integrated signal on distance z_1 between the targets for electron energy $\epsilon = 1$ GeV and $2\theta_B = \pi$. Integration over ω is made in the range $\omega_{\rm PXR} \pm 2$ eV. Acceptance angle is $2/\gamma$ (lower solid line) and $4/\gamma$ (upper solid line). Dashed lines: corresponding asymptotic values at $z_1 \gg l_v$.

The figures show the angular distribution of radiation spectral intensity (28) at frequency $\omega_{\rm PXR}$ corresponding to the direction $\theta = 2\theta_B$. Presently, ϑ is the angle between observation direction and $-\boldsymbol{v}$. Let us note that it is monochromatic peaks that are presented here, not the reflexes. Nevertheless, each distribution on Fig. 7 coincides with the corresponding reflex. The reason for this is rather large peak width (15) at $2\theta_B = \pi$ comparing to characteristic width $\sim\gamma^{-1}$ of the reflex. The situation is nearly the same on Fig. 6 where small discrepancies appear only at $\vartheta > \omega_p/\omega$ (as for solid line on the right part of Fig. 3).

With the further increase of z_1 beyond the l_v value the cosine and the exponent in parentheses in (28) become quickly oscillating functions of ϑ (as well as ω). Therefore, at $z_1 \gg l_v$ it is reasonable to consider distribution averaged over small intervals of ϑ, which corresponds to substitution $e^{-iz_1/l_v}, \cos(z_1/l_v) \to 0$. The dotted-dashed line on Fig. 8 shows such asymptotic average distribution. It appears to have maximum in the same direction ($\vartheta = \gamma^{-1}$) as the distribution (13) for electron with Coulomb field in an ultrathin target (dashed line), however, exceeds it by intensity. Such additional intensity comes from TR, produced during the electron exit from the upstream target [second term in (23)] and diffracted in the downstream one. The solid line shows the example of nonaveraged distribution for $z_1 = 2.5 l_v$.

Let us now consider the evolution of the signal, integrated with respect to frequency and observation angle, with the increase of the distance z_1 between the targets. For simplicity, we will, as previously, focus on the axially symmetrical case $2\theta_B = \pi$. The results have analogous form for various other crystal orientations (e.g., Laue geometry, which might be more preferable for experimental study) since they primarily reflect the evolution of the field surrounding the impinging electron with the increase of z.

As far as frequency integration is concerned, the contributing interval depends on the corresponding interval of angular integration. From the relation (8) it follows that for a high-energy electron under considered conditions, the change of the $\omega_{\rm PXR}$ value by about 1 eV is caused by deviation of the observation angle (from $\vartheta = 0$) by 0.035 rad. Meanwhile, the characteristic width of the pulse has the scale of $\sim\eta_p/\omega$, which is ~0.01 in the considered case. Therefore, presently the change of the resonance frequency can be neglected and the effective region of numerical integration of (28) is defined by the peak width (Fig. 4), which is about several eV around the value $\omega_{\rm PXR}(0)$. Let us note that the situation may be different at smaller θ_B values due to more rapid change of $\omega_{\rm PXR}$ with the angle in this case.

Figure 9 shows the dependence of the integrated signal on z_1 for the electron energy $\epsilon = 1$ GeV and two values of integration range with respect to angle ϑ. The dimensionless value $W_{\rm int}$ is defined here as

$$W_{\rm int} = \frac{10^{-5} 4\pi^2}{e^2\omega^2|n_{\mathbf{g}}|^2 L^2} \int d\omega \int_0^{\vartheta_0} 2\pi\vartheta\, d\vartheta \frac{d^2W}{d\omega\, do}. \qquad (29)$$

By the acceptance angle in Fig. 9 we mean the doubled value $2\vartheta_0$ of the upper limit in the angle integral in (29), i.e., the cone angle corresponding to the solid one which comprises the considered part of the reflex. The figure shows that with the increase of the distance between the targets up to several values of l_v, which is ≈0.23 mm for $\vartheta = \gamma^{-1}$ in the present case, the signal monotonically increases. With the further increase of z_1 it is possible to observe the decrease of the signal and its damping oscillatory behavior in the vicinity of the asymptote. Such behavior is a remnant of full-amplitude oscillations (from zero to the maximum value) of the cosine and the exponent in (28), which is partially blurred by angle integration (frequency integration alone does not affect oscillations due to high degree of the pulse monochromaticity). The discussed behavior, particularly, the signal decrease with the increase of z_1, could be observed for acceptance angles not exceeding several γ^{-1} values which is a quite achievable (experimentally) scale in the considered case.

With the increase of the electron energy the formation length l_v grows very quickly at sufficiently small values of ϑ. In this case, the intensity of x-ray emission from the downstream target can depend on z_1 within macroscopically large values of this distance. Such situation is depicted on Fig. 10 for the case $\epsilon = 100$ GeV. Here, we choose the acceptance angle values to equal $200/\gamma$ and $600/\gamma$, which are, respectively, 1 and 3 mrad in the considered case. Presently, all the oscillations are almost removed by integration up to $\vartheta_0 \gg \gamma^{-1}$ and we obtain

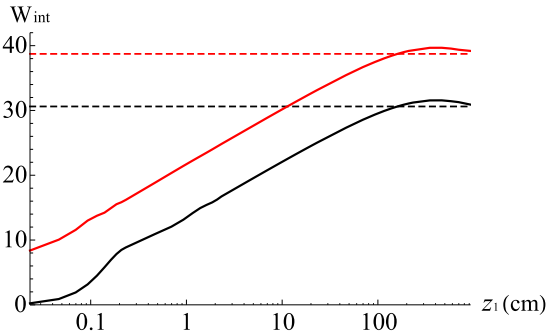

FIG. 10. Dependence of the integrated signal on distance z_1 between the targets for electron energy $\epsilon = 100$ GeV and $2\theta_B = \pi$. Integration over ω is made in the range $\omega_{\rm PXR} \pm 2$ eV. Acceptance angle is $200/\gamma = 1$ mrad (lower solid line) and $600/\gamma = 3$ mrad (upper solid line). Dashed lines: corresponding asymptotic values at $z_1 \gg l_v$.

monotone logarithmic increase of the signal within the distance of about several meters (here, $l_v \approx 230$ cm at $\vartheta = 1/\gamma$).

Let us note that the considered here effect of x-ray pulse intensity dependence on distance between the targets has analogs in the processes of ionization loss by high-energy electrons and electron-positron pairs in the system of two targets [57,58].

C. On bremsstrahlung contribution

In the considered statement of the problem, which involves two targets, the electron generates bremsstrahlung both in the upstream and the downstream targets, which can diffract in the downstream one and contribute to the measured x-ray pulse. In order to roughly estimate the relative value of such contribution, it is enough to consider bremsstrahlung from the upstream (much thicker) target.

Due to Ter-Mikaelyan density effect [1], the characteristic angular distribution of bremsstrahlung in this case has the width $\sim\eta_p/\omega$ instead of $1/\gamma$. It coincides (or is at least of the same order of magnitude for a crystal with different plasma frequency) with the corresponding angular width of PXR reflex generated by the electron's proper field partially screened by polarization. Thus, the ratio of contributions of the considered two types of radiation to the x-ray pulse in the present case can be judged from the comparison of the spectral-angular density of bremsstrahlung impinging upon the downstream target with such density of the equivalent photon flux associated with the screened Coulomb field. At $\gamma \gg 1$ in the considered frequency range the discussed bremsstrahlung density can be presented as follows [31]:

$$\frac{d^2W}{d\omega\, do} = \frac{2\xi^2 d}{\pi\gamma^2 X_0}\left[1 - 2\theta_v^2\xi^2\left(\xi^{-1} - \theta_v^2\right)\right], \qquad (30)$$

where $\xi = 1/(\gamma^{-2} + \theta_v^2 + \eta_p^2/\omega^2)$, θ_v is the emission angle with respect to the electron velocity, d is the upstream target thickness, and X_0 is the radiation length. The Planck constant $\hbar$ is put here to equal unit. The expression (30) should be rather considered as an upper bound for $d^2W/d\omega\, do$ since it does not take into account additional (however, much weaker than the one by the density effect) suppression by Landau-Pomeranchuk-Migdal effect [41–44].

The corresponding density of the equivalent photon flux is (see, e.g., [13,20])

$$\frac{d^2W}{d\omega\, do} \approx \frac{\alpha}{\pi^2}\theta_v^2\xi^2, \qquad (31)$$

where α is the fine-structure constant.

In order to compare the values of (30) and (31), it is natural to choose the maxima of these distributions corresponding to the emission angle (with respect to the electron velocity) $\theta_v = 0$ for bremsstrahlung and to $\theta_v = \eta_p/\omega$ for virtual photons (at $\gamma \gg \omega/\eta_p$). Let us make estimation for a silicon target ($X_0 \approx 10$ cm) of thickness $d = 10$ μm, electron energy $\epsilon = 1$ GeV, and radiation frequency $\omega = 3$ keV. The ratio of (30) to (31) in this case is extremely small and amounts to about 10^{-3}. With the increase of ϵ this value decreases as $1/\epsilon^2$. Such result is in accordance with the fact (see, i.e., [60]) that under condition $\gamma \gg \omega/\omega_p$ (with ω_p being the plasma frequency of the crystal) the intensity of diffracted bremsstrahlung is negligible comparing to the one of PXR produced in the same target. The presented estimation shows that under conditions considered in the present section, this is valid for the intensity of bremsstrahlung from the thick upstream target as well, which can therefore be neglected.

Let us note that the way applied here to compare PXR and diffracted bremsstrahlung intensities via the intensities impinging upon the crystal is valid due to sufficiently small thickness of the crystalline target (smaller than the extinction length).

IV. EFFECT OF THE DOWNSTREAM TARGET FINITENESS

Previously, we studied the evolution of x-ray pulse characteristics with the change of the distance between the targets considering the radiating downstream target as infinite in transversal (orthogonal to z axis) directions. In this case, the asymptotic value of the reflex intensity at $z_1 \gg l_v$ exceeds the corresponding value (13) for an impinging electron with Coulomb field (in the absence of the upstream target). This happens due to the contribution of TR from the upstream target which is diffracted by the infinite downstream target at arbitrary z_1. The situation is different for a crystalline target finite in transversal direction, which can be partially missed by such TR waves at rather large z_1. Let us now study the process of the reflex intensity tending (with the increase of z_1) to the expected value typical for the electron with Coulomb field, associated with the finiteness of the crystalline target transversal size.

For the present purpose, it is convenient to write the field (24) inside the downstream target as an explicit sum of contributions associated with the electron proper Coulomb field in vacuum and TR generated upon the particle exit from the upstream target:

$$\mathbf{E}_\omega^{(0)}(\mathbf{r}) = -\frac{ie}{\pi}\int d^2q\, \mathbf{q}\{Q_c' e^{i\frac{\omega z_1}{v}} - Q_f' e^{iz_1\sqrt{\omega^2-q^2}}\}e^{i(z-z_1)\sqrt{\omega^2\varepsilon_0-q^2}+i\mathbf{q}\cdot\boldsymbol{\rho}}. \qquad (32)$$

Such form of the expression (24) is valid in the crystals satisfying the condition (12), which we presently consider. For simplicity, we will consider a circular downstream target with the radius R. Let us derive the expression for radiation spectral-angular density on the basis of (5), with (32) as a leading-order solution, for such case.

The integrand in (5), as previously, contains two exponents, $e^{iq_f z'}$ and $e^{i\boldsymbol{\rho}'\cdot(\mathbf{q}-\boldsymbol{\kappa}_\perp)}$, which are subject to integration with respect to z' and $\boldsymbol{\rho}'$, respectively (let us note that the quantity q_f contains here the variable q instead of $\kappa_\perp$, which it had in previous sections, since presently there is no delta function $\delta(\mathbf{q}-\boldsymbol{\kappa}_\perp)$ to perform immediate integration over $\mathbf{q}$). Naturally, only the second integration makes the present case different from that of $R\to\infty$, leading to

$$\int d^2\rho' e^{i\boldsymbol{\rho}'\cdot(\mathbf{q}-\boldsymbol{\kappa}_\perp)} = 2\pi R\frac{J_1(|\mathbf{q}-\boldsymbol{\kappa}_\perp|R)}{|\mathbf{q}-\boldsymbol{\kappa}_\perp|} \tag{33}$$

instead of $(2\pi)^2\delta(\mathbf{q}-\boldsymbol{\kappa}_\perp)$. It is also possible to replace the combination $e^{iLq_f/2}S_f$ appearing in the result of integration with respect to z' by $e^{iLq_c/2}S_c$ (due to condition $L|q_f-q_c|\ll 1$, see Sec. II), which does not depend on q. In the result for the radiation field we obtain

$$\mathbf{E}'_\omega(\mathbf{r}) = \frac{ieR}{2\pi}\frac{e^{ikr}}{r}S_c n_{\mathbf{g}} e^{i(Lq_c/2-z_1\kappa_z)}\mathbf{k}\times[\mathbf{k}\times\mathbf{I}_R], \tag{34}$$

where

$$\mathbf{I}_R = \int d^2q\,\mathbf{q}\frac{J_1(|\mathbf{q}-\boldsymbol{\kappa}_\perp|R)}{|\mathbf{q}-\boldsymbol{\kappa}_\perp|}\left\{Q'_c e^{i\frac{\omega z_1}{v}} - Q'_f e^{iz_1\sqrt{\omega^2-q^2}}\right\}. \tag{35}$$

The first term in (35) is associated with the Coulomb field in vacuum (18). Thus, the value of R below which the finiteness of the target is not negligible for this term can be defined as $R\sim\gamma/\omega$. In x-ray region this value is rather small even at large particle energies (i.e., for 100 GeV it reaches $\sim 10^{-3}$ cm for several keV photon energies) and in practice the target size significantly exceeds it. For $z_1 < l_v$, the same situation takes place for the total field (34) as well. In this case, the major part of the energy of the field around the half-bare electron is concentrated within the distance $\rho\sim\sqrt{z/\omega} < \gamma/\omega$. This makes the values of R at which the condition $R\to\infty$ is inapplicable even smaller than in the case of a particle with Coulomb field. Thus, the results presented in the previous sections remain intact for the targets of $R\gg\gamma/\omega$ and further we will concentrate on the case $z_1\gg l_v$.

For the discussed values of z_1, the typical values of $\kappa_\perp$ should be considered as $\kappa_\perp\sim\omega/\gamma$, which correspond to the characteristic angular width $\sim\gamma^{-1}$ of the reflex in this case. For the targets of $R\gg\gamma/\omega$, the expression (34) for the radiation field can be further simplified. In this case, in the first term in (35) the structure (33) can be replaced by delta function and the corresponding part of (35) gains the form

$$\frac{2\pi}{R}\frac{\boldsymbol{\kappa}_\perp}{\kappa_\perp^2+\eta^2/\gamma^2}e^{i\frac{\omega}{v}z}. \tag{36}$$

As far as the second term is concerned, let us, as previously, expand here the square root in the exponent in small parameter q/ω and make a substitution $\mathbf{q}=\mathbf{u}+\boldsymbol{\kappa}_\perp$. The values u_{eff} of u contributing to the integral here do not significantly exceed $1/R$ due to the presence of $J_1(uR)$ in the integrand (they are likely to be even less due to the presence of the exponent). Under condition $R\gg\gamma/\omega$, this means $u_{eff}\ll\omega/\gamma\sim\kappa_\perp$. Thus, the vector $\mathbf{u}$ can be neglected comparing to $\boldsymbol{\kappa}_\perp$ in the integrand (excluding the exponent). This allows to calculate analytically the integral with respect to angle between $\mathbf{u}$ and $\boldsymbol{\kappa}_\perp$ and present the corresponding part of the radiation field (35) in the form

$$-\frac{2\pi}{R}\frac{\boldsymbol{\kappa}_\perp\omega_p^2 e^{i\omega z_1(1-\kappa_\perp^2/2\omega^2)}}{(\kappa_\perp^2+\omega^2/\gamma^2)(\kappa_\perp^2+\omega^2/\gamma^2+\omega_p^2)}F_R, \tag{37}$$

where the function

$$F_R = R\int_0^\infty du\,J_1(uR)J_0(uz_1\kappa_\perp/\omega)e^{-iz_1u^2/2\omega} \tag{38}$$

depends on ω, R, z_1, and the observation angle ϑ. Figure 11 shows (solid line) the example of z_1 dependence for $|F_R|$ for $\epsilon=200$ MeV and $\vartheta=\gamma^{-1}$ for ω_{PXR} frequency (8). The diameter of the target is chosen to equal 0.5 cm. As previously we dwell on the case $2\theta_B=\pi$ and put $\kappa_\perp=\omega\vartheta$. The figure shows that at $z\approx R/\vartheta$ the contribution (37) of TR into radiation field rapidly drops. At smaller z_1, the value of $|F_R|$ is close to unit and the finiteness of the target does not play any role. The rapid oscillations here originate from the exponent in the integrand of (38). Such oscillations are blurred after integration with respect to ϑ and ω. Moreover at $z_1\gg l_v$, which is presently the case, the value of the exponent under discussion remains close to unit in the region of u, making the main contribution to (38). Therefore, further we will substitute $e^{-iz_1u^2/2\omega}\to 1$, which allows to calculate the integral in (38) analytically and obtain

$$F_R\approx\theta(R\omega/\kappa_\perp - z_1), \tag{39}$$

where $\theta(x)$ is the Heaviside θ function which equals unit for $x>0$ and zero for $x<0$. The dependence (39) is presented on Fig. 11 by the dashed line.

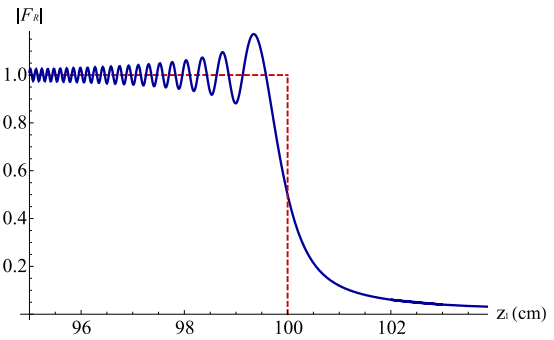

FIG. 11. Dependence (38) (solid line) and (39) (dashed line) of $|F_R|$ on z_1 in the vicinity of $z_1=R/\vartheta=100$ cm. Here, $\gamma=400$, $R=0.25$ cm, $\vartheta=\gamma^{-1}$, $\omega\approx 3.228$ keV, $2\theta_B=\pi$.

With the use of (6), (34), (36), and (37) the expression for radiation spectral-angular density from the finite target can be obtained ($z_1\gg l_v$):

$$\frac{d^2W}{d\omega\,do} = \frac{e^2\omega^2}{4\pi^2}|n_{\mathbf{g}}|^2|\mathbf{k}\times\boldsymbol{\kappa}_\perp|^2 S_c^2\left\{K'^2_c + K_f^2|F_R|^2\right\}. \tag{40}$$

We neglect here the term describing the interference between the fields (36) and (37), which at such large z_1 is a rapidly oscillating function of $\kappa_\perp$ and ω and vanishes at averaging over small intervals of these values.

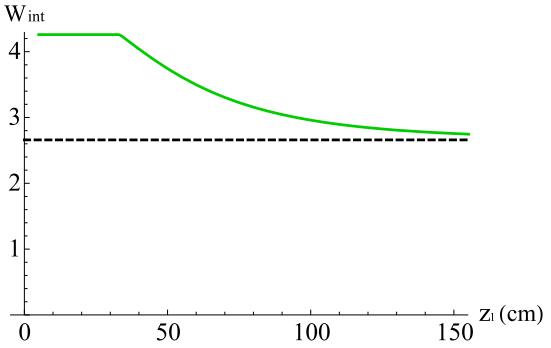

FIG. 12. Dependence of the integrated signal on distance z_1 between the targets for electron energy $\epsilon = 200$ MeV, $R = 0.25$ cm, and $2\theta_B = \pi$. Integration over ω is made in the range $\omega_{\rm PXR} \pm 3$ eV. Acceptance angle $2\vartheta_0 \approx 6/\gamma \approx 15$ mrad. Dashed line: corresponding asymptotic value at $z_1 \gg R/\vartheta_0$.

Figure 12 shows the dependence of the yield (40) integrated with respect to ω and ϑ for the acceptance angle $2\vartheta_0 \approx 6/\gamma$. The electron energy is chosen to equal 200 MeV. The considerations analogous to the ones presented in Sec. III B show that presently it is enough to integrate with respect to ω in the interval $\omega_{\rm PXR} \pm 3$ eV in order to take into account almost all the radiated energy in the chosen angular region. In the considered case, the formation length l_v at $\vartheta = \gamma^{-1}$ equals only about 10 μm. The figure shows that the finiteness of the downstream target results in the dependence of the radiation yield on distance between the targets for the values of this distance of the order of l_R, which is much larger than l_v. This distance can be macroscopically large even for not very high energies of the electron (as the one chosen on Fig. 12). For a certain value of the acceptance angle $2\vartheta_0$ the decrease of the signal begins at $z_1 = R/\vartheta_0$. Since at the considered distances ($z_1 \gg l_v$) significant amount of radiated energy is concentrated at $\vartheta \sim \gamma^{-1}$, the upper estimation of the distance on which the x-ray reflex intensity decreases is $l_R \sim R\gamma$. With the increase of z_1 within l_R the yield gradually changes from the asymptotic ($z \gg l_v$) value for an infinite downstream target [obtained from (29) and (26) with $e^{-iz_1/l_v} \to 0$] to the one typical for an electron with Coulomb field impinging upon a single infinite ultrathin target [obtained from (29) and (13)]. The difference between these yields [corresponding to (13) and (26)] grows with the increase of the electron energy.

Let us note that the sharp change of $dW_{\rm int}/dz_1$ at $z_1 = R/\vartheta_0 = 100$ cm on Fig. 12 is attributed to the approximate form (39) of the function F_R, corresponding to the treatment of TR from the upstream target in the framework of geometrical optics. Presently, the value $z_1 = R/\vartheta_0$ is the minimum one at which the finiteness of the target begins being manifested.

V. CONCLUSIONS

In this paper we considered the process of x-ray emission by an ultrarelativistic electron which normally crosses the system of two targets in vacuum separated by distance z_1. The upstream target was assumed to be thick and amorphous (having plasma frequency η_p) while the downstream one ultrathin and crystalline (with plasma frequency ω_p). It is the radiation originated from the Bragg diffraction of the electromagnetic field around the impinging electron in the downstream target that was investigated (interfering sum of PXR and DTR). Due to the electron preliminary traversal of the upstream target, this field gradually evolves with the increase of the distance from the target, which results in TR formation. The stages of such evolution are described in detail.

At sufficiently high electron energies, the field evolution takes place within macroscopically large distance $l_v \sim \gamma^2/\omega$ and manifests itself in characteristics of the x-ray pulse produced by the particle in the ultrathin downstream target. In this case at $z_1 < \omega/\eta_p^2$ these characteristics are typical for PXR from a thick crystal, having the same plasma frequency η_p as the amorphous target, the characteristic width of the reflex angular distribution being $\sim\eta_p/\omega$ and its yield being independent on the electron energy. With the increase of z_1 at $z_1 < l_v$, both the angular distribution and radiation yield change and are not typical for x-ray pulse neither from thick nor from ultrathin crystals. At $z_1 \gg l_v$, the angular distribution acquires its final form (in the approximation of infinite transversal size of the crystalline target) with characteristic angular width $\sim\gamma^{-1}$ typical for ultrathin targets, however, the radiation yield still exceeds the corresponding value for an impinging electron with Coulomb field. It happens due to additional contribution of TR generated upon the particle exit from the upstream target.

In Sec. IV the influence of the finiteness of the downstream target transversal size upon radiation characteristics is studied. It is shown that in practice in the considered process such finiteness manifests itself on distances $z_1 \gg l_v$ which can be macroscopically large even at not very high electron energies. It results in observable change of the radiation yield with the increase of z_1 at such distances, as a result of which the mentioned additional TR contribution vanishes.

ACKNOWLEDGMENTS

The work was partially supported by the Projects No. 0117U004866 of the Ministry of Education and Science of Ukraine and the Projects No. F56/2018 and C-2/50-2018 of the National Academy of Sciences of Ukraine. The author is grateful to A. V. Shchagin and N. F. Shul'ga for useful discussions and valuable remarks.

[1] M. L. Ter-Mikaelyan, *High-Energy Electromagnetic Processes in media* (Wiley, New York, 1972); in Russian the book is published in 1969.

[2] S. V. Bazylev and N. K. Zhevago, *Radiation by Fast Particles in Substance and External Fields* (Nauka, Moscow, 1987).

[3] A. I. Akhiezer and N. F. Shul'ga, *High Energy Electrodynamics in Matter* (Gordon and Breach, Amsterdam, 1996).

[4] P. Rullhusen, X. Artru, and P. Dhez, *Novel Radiation Sources using Relativistic Electrons: From Infrared to x-rays* (World Scientific, Singapore, 1998).

[5] A. P. Potylitsyn, *Electromagnetic Radiation of Electrons in Periodic Structures* (Springer, Berlin, 2011).

[6] Y. B. Fainberg and N. A. Khizhnyak, Zh. Eksp. Teor. Fiz. **32**, 883 (1957) [Sov. Phys. JETP **5**, 720 (1957)].

[7] H. Nitta, Phys. Lett. A **158**, 270 (1991).

[8] G. M. Garibian and C. Yang, Zh. Eksp. Teor. Fiz. **61**, 930 (1971) [Sov. Phys. JETP **34**, 495 (1972)].

[9] V. G. Baryshevsky and I. D. Feranchuk, Zh. Eksp. Teor. Fiz. **61**, 944 (1971) [Sov. Phys. JETP **34**, 502 (1972)].

[10] S. A. Vorobiev, B. N. Kalinin, S. Pak, and A. P. Potylitsyn, Pis'ma Zh. Eksp. Teor. Fiz. **41**, 3 (1985) [JETP Lett. **41**, 1 (1985)].

[11] Y. N. Adishchev, A. N. Didenko, V. V. Mun, G. A. Pleshkov, A. P. Potylitsyn, V. K. Tomchakov, S. R. Uglov, and S. A. Vorobiev, Nucl. Instrum. Methods Phys. Res., Sect. B **21**, 49 (1987).

[12] J. Freudenberger, V. B. Gavrikov, M. Galemann, H. Genz, L. Groening, V. L. Morokhovskii, V. V. Morokhovskii, U. Nething, A. Richter, J. P. F. Sellschop, and N. F. Shul'ga, Phys. Rev. Lett. **74**, 2487 (1995).

[13] A. V. Shchagin and X. K. Maruyama, in *Accelerator-based Atomic Physics Techniques and Applications*, edited by S. M. Shafroth and J. C. Austin (AIP Press, New York, 1997), pp. 279–307.

[14] V. L. Morokhovskii, *The Coherent X-Radiation of Relativistic Electrons in a Crystal* (CNII Atominform, Moscow, 1989).

[15] A. N. Aleinik, A. N. Baldin, E. A. Bogomazova, I. E. Vnukov, B. N. Kalinin, A. S. Kubankin, N. N. Nasonov, G. A. Naumenko, A. P. Potylitsyn, and A. F. Sharafutdinov, JETP Lett. **80**, 393 (2004).

[16] H. Backe, A. Rueda, W. Lauth, N. Clawiter, M. El-Ghazaly, P. Kunz, and T. Weber, Nucl. Instrum. Methods Phys. Res., Sect. B **234**, 138 (2005).

[17] V. G. Baryshevsky, Nucl. Instrum. Methods Phys. Res., Sect. B **122**, 13 (1997).

[18] A. Kubankin, N. Nasonov, V. Sergienko, and I. Vnukov, Nucl. Instrum. Methods Phys. Res., Sect. B **201**, 97 (2003).

[19] A. V. Shchagin, V. I. Pristupa, and N. A. Khizhnyak, Phys. Lett. A **148**, 485 (1990).

[20] X. Artru and P. Rullhusen, Nucl. Instrum. Methods Phys. Res., Sect. B **145**, 1 (1998), addendum **173**, 16 (2001).

[21] A. V. Shchagin, Phys. Usp. **58**, 819 (2015).

[22] A. Caticha, Phys. Rev. A **40**, 4322 (1989).

[23] A. P. Potylitsyn and V. A. Verzilov, Phys. Lett. A **209**, 380 (1995).

[24] S. V. Blazhevich and A. V. Noskov, Zh. Eksp. Teor. Fiz. **147**, 875 (2015) [JETP **120**, 753 (2015)].

[25] I. Chaikovska, R. Chehab, X. Artru, and A. V. Shchagin, Nucl. Instrum. Methods Phys. Res., Sect. B **402**, 75 (2017).

[26] A. Gogolev, A. Potylitsyn, and G. Kube, J. Phys.: Conf. Ser. **357**, 012018 (2012).

[27] Y. Takabayashi, Phys. Lett. A **376**, 2408 (2012).

[28] Y. Takabayashi and K. Sumitani, Phys. Lett. A **377**, 2577 (2013).

[29] N. N. Nasonov, Phys. Lett. A **246**, 148 (1998).

[30] B. M. Bolotovsky, Proc. (Tr.) P. N. Lebedev Phys. Inst. **140**, 95 (1982), in Russian.

[31] V. L. Ginzburg and V. N. Tsytovich, *Transition Radiation and Transition Scattering* (Adam Hilger, Bristol, 1984).

[32] G. M. Garibian, Zh. Eksp. Teor. Fiz. **37**, 527 (1959) [Sov. Phys. JETP **10**, 372 (1960)].

[33] A. I. Alikhanian, G. M. Garibian, M. P. Lorikian, A. K. Valter, I. A. Grishaev, V. A. Petrenko, and G. L. Fursov, Zh. Eksp. Teor. Fiz. **44**, 1122 (1963) [Sov. Phys. JETP **17**, 756 (1963)].

[34] A. I. Alikhanian, A. K. Valter, G. M. Garibian, I. A. Grishaev, M. P. Lorikian, V. A. Petrenko, and G. L. Fursov, Zh. Eksp. Teor. Fiz. **46**, 1212 (1964) [Sov. Phys. JETP **19**, 820 (1964)].

[35] A. H. Sorensen, Phys. Rev. A **36**, 3125 (1987).

[36] G. M. Garibian and S. Yan, *X-ray Transition Radiation* (Publ. of Arm. SSR Acad. Sci., Yerevan, 1983).

[37] S. V. Trofymenko and N. F. Shul'ga, Phys. Rev. Accel. Beams **19**, 112801 (2016).

[38] E. L. Feinberg, Zh. Eksp. Teor. Fiz. **50**, 202 (1966) [Sov. Phys. JETP **23**, 132 (1966)].

[39] E. L. Feinberg, UFN **132**, 255 (1980) [Sov. Phys. Usp. **23**, 629 (1980)].

[40] N. F. Shul'ga and S. P. Fomin, Phys. Lett. A **114**, 148 (1986).

[41] L. D. Landau and I. Y. Pomeranchuk, Dokl. Akad. Nauk SSSR **92**, 535 (1953) [*Collected papers of L. D. Landau*, edited by D. Ter Haar (Pergamon Press, Oxford, 1965), p. 589].

[42] A. B. Migdal, Phys. Rev. **103**, 1811 (1956).

[43] P. L. Anthony, R. Becker-Szendy, P. E. Bosted, M. Cavalli-Sforza, L. P. Keller, L. A. Kelley, S. R. Klein, G. Niemi, M. L. Perl, L. S. Rochester, and J. L. White, Phys. Rev. Lett. **75**, 1949 (1995).

[44] S. Klein, Rev. Mod. Phys. **71**, 1501 (1999).

[45] F. F. Ternovsky, Zh. Eksp. Teor. Fiz. **39**, 171 (1960) [Sov. Phys. JETP **12**, 123 (1961)].

[46] N. F. Shul'ga and S. P. Fomin, Pis'ma Zh. Eksp. Teor. Fiz. **27**, 126 (1978) [JETP Lett. **27**, 117 (1978)].

[47] H. D. Thomsen, J. Esberg, K. Kirsebom, H. Knudsen, E. Uggerhoj, U. I. Uggerhoj, P. Sona, A. Mangiarotti, T. J. Ketel, A. Dizdar, M. M. Dalton, S. Ballestrero, and S. H. Connell, Phys. Lett. B **672**, 323 (2009).

[48] H. D. Thomsen, J. Esberg, K. K. Andersen, M. D. Lund, H. Knudsen, U. I. Uggerhoj, P. Sona, A. Mangiarotti, T. J. Ketel, A. Dizdar, S. Ballestrero, and S. H. Connell, Phys. Rev. D **81**, 052003 (2010).

[49] U. I. Uggerhoj, Rev. Mod. Phys. **77**, 1131 (2005).

[50] G. Naumenko, X. Artru, A. Potylitsyn, Y. Popov, L. Sukhikh, and M. Shevelev, J. Phys.: Conf. Ser. **236**, 012004 (2010).

[51] G. Naumenko, Y. Popov, and M. Shevelev, J. Phys.: Conf. Ser. **357**, 012005 (2012).

[52] X. Artru and C. Ray, Nucl. Instrum. Methods Phys. Res., Sect. B **266**, 3725 (2008).

[53] X. Artru, Il Nuovo Cimento C **34**, 29 (2011).

[54] Y. Shibata, K. Ishi, T. Takahashi, T. Kanai, F. Arai, S. I. Kimura, T. Ohsaka, M. Ikezawa, Y. Kondo, R. Kato, S. Urasawa, T. Nakazato, S. Niwano, M. Yoshioka, and M. Oyamada, Phys. Rev. E **49**, 785 (1994).

[55] N. F. Shul'ga, S. V. Trofymenko, and V. V. Syshchenko, Pis'ma Zh. Eksp. Teor. Fiz. **93**, 3 (2011) [JETP Lett. **93**, 1 (2011)].

[56] S. V. Trofymenko, N. F. Shul'ga, N. Delerue, S. Jenzer, V. Khodnevych, and A. Migayron, J. Phys.: Conf. Ser. **874**, 012076 (2017).

[57] N. F. Shul'ga and S. V. Trofymenko, Phys. Lett. A **376**, 3572 (2012).

[58] S. V. Trofymenko and N. F. Shul'ga, Nucl. Instrum. Methods Phys. Res., Sect. B **402**, 44 (2017).

[59] A. Erdelyi, *Asymptotic Expansions* (Dover Publications, New York, 1956).

[60] Y. A. Goponov, S. A. Laktionova, M. A. Sidnin, and I. E. Vnukov, Nucl. Instrum. Methods Phys. Res., Sect. B **402**, 92 (2017).